



# Barium doping effect on the photovoltaic performance and stability of $\text{MA}_{0.4}\text{FA}_{0.6}\text{Ba}_x\text{Pb}_{1-x}\text{I}_y\text{Cl}_{3-y}$ perovskite solar cells

Shun-Hsiang Chan<sup>a,b,1</sup>, Ming-Chung Wu<sup>a,b,c,\*</sup>, Yi-Ying Li<sup>a</sup>, Kun-Mu Lee<sup>a,b,c</sup>, Yang-Fang Chen<sup>d</sup>, Wei-Fang Su<sup>e,\*</sup>

<sup>a</sup> Department of Chemical and Materials Engineering, Chang Gung University, Taoyuan 33302, Taiwan

<sup>b</sup> Green Technology Research Center, Chang Gung University, Taoyuan 33302, Taiwan

<sup>c</sup> Division of Neonatology, Department of Pediatrics, Chang Gung Memorial Hospital, Linkou, Taoyuan 33305, Taiwan

<sup>d</sup> Department of Physics, National Taiwan University, Taipei 10617, Taiwan

<sup>e</sup> Department of Materials Science and Engineering, National Taiwan University, Taipei 10617, Taiwan

## ARTICLE INFO

### Keywords:

Perovskite solar cell  
Barium dopant  
Power conversion efficiency  
In-situ GIWAXS  
J-V hysteresis

## ABSTRACT

Perovskite solar cells (PSCs) have earned widespread attention owing to its fast-growing power conversion efficiency (PCE). However, there are some challenges for this type of solar cells. The toxicity issue, current density-voltage (J-V) hysteresis, and uncertain stability hinder commercialization. In this study, we developed the PSCs with  $\text{MA}_{0.4}\text{FA}_{0.6}\text{Ba}_x\text{Pb}_{1-x}\text{I}_y\text{Cl}_{3-y}$  film as active layer. The  $\text{MA}_{0.4}\text{FA}_{0.6}\text{Ba}_x\text{Pb}_{1-x}\text{I}_y\text{Cl}_{3-y}$  film with various barium doping concentrations were fabricated by solvent engineering method. We investigate the surface morphology, crystal orientation, and optical property of various perovskite films. Furthermore, the in situ grazing-incidence wide-angle X-ray scattering (in-situ GIWAXS) is used to analyze the heating crystallization process of perovskite film. We discover that Ba can improve crystallinity and structural stability. For the optimal 5.0 mol% Ba replacement, the PCE of perovskite device is increased to 17.4%, the J-V hysteresis can be completely eliminated and the device demonstrates long-term stability.

## 1. Introduction

Perovskite solar cells (PSCs), a highly-efficient photovoltaic technology, is considered to be the most promising renewable energy sources in the 21st century, owing to its rapidly improved power conversion efficiency (PCE). Since T. Miyasaka group published the PSCs with PCE of 3.8% in 2009 [1], a great deal of effort has been devoted to transporting material design, interfacial engineering, composition engineering for pursuing highly-efficient PSCs [2–10]. To date, the PCE of PSC is successfully raised to 25.2% by KRICT/MIT and Korea University [11]. The outstanding photovoltaic performance dramatically improves the commercialization potential of PSCs.

As we know, PSCs contain harmful element lead (Pb) that increases environmental damage, and also presents many difficulties for the factory to mass-produce. Moreover, long-term exposure to lead has a wide range of effects on a child's development [12]. It is imperative to develop Pb-free or Pb-reduced perovskite to improve the competitiveness of PSC [13–20]. When pursuing the alternatives for the toxic lead,

many factors need to be concerned. For the stability of the perovskite structure, the size of the ionic radius should be considered. According to the role of Goldschmidt's tolerance factor and octahedral factor, the divalent metal ions, such as tin (Sn) [21–23], germanium (Ge) [24], calcium (Ca) [25,26], strontium (Sr) [27–29], barium (Ba) [29,30], etc [31,32] can be seen as the candidate for replacing Pb in perovskite unit cell. To date, many research groups demonstrated Sn-based PSC with the PCE of ~10%. Nevertheless, the strong oxidizing property of  $\text{Sn}^{2+}$  to  $\text{Sn}^{4+}$  extremely degrades the stability of PSCs [18,33].

Partial substitution of Pb by divalent metal ion has attracted great interest to achieve environmental protection and to enhance PSC performance. L. Ji *et al.* demonstrated that the Pb-Sn mixed triple cation PSC shows a high PCE of 16.10% without hysteresis phenomenon because of the optimized band alignment [34]. X. Du *et al.* reported that  $(\text{FASnI}_3)_{0.6}(\text{MAPbI}_3)_{0.4}$  solar cells exhibited PCE of 14.56% by  $\text{Me}_4\text{NBr}$  surface treatment [35]. C. Lu *et al.* partially replaced Pb by Ca and they found that 0.1%  $\text{Ca}^{2+}$  incorporation could enhance the photovoltage and photocurrent of the device [36]. P. Caprioglio *et al.* demonstrated

\* Corresponding authors at: Department of Chemical and Materials Engineering, Chang Gung University, Taoyuan 33302, Taiwan (M.-C. Wu). Department of Materials Science and Engineering, National Taiwan University, Taipei 10617, Taiwan (W.-F. Su).

E-mail addresses: [mingchungwu@cgu.edu.tw](mailto:mingchungwu@cgu.edu.tw) (M.-C. Wu), [suwf@ntu.edu.tw](mailto:suwf@ntu.edu.tw) (W.-F. Su).

<sup>1</sup> These authors contributed equally to this work.

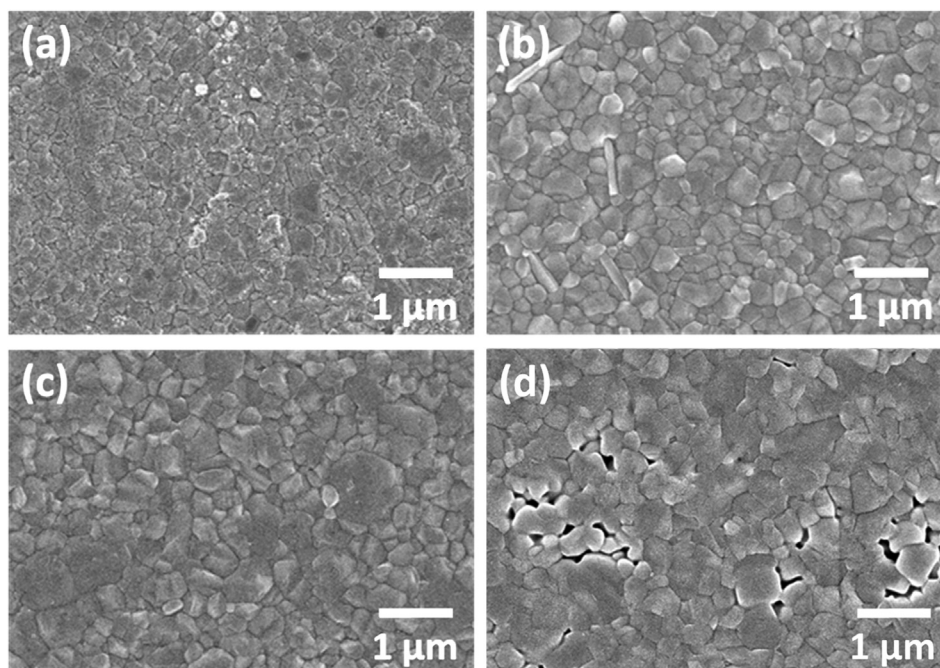


Fig. 1. FE-SEM images of (a)  $\text{MA}_{0.4}\text{FA}_{0.6}\text{PbI}_y\text{Cl}_{3-y}$ , (b)  $\text{MA}_{0.4}\text{FA}_{0.6}\text{Ba}_{0.03}\text{Pb}_{0.97}\text{I}_y\text{Cl}_{3-y}$ , (c)  $\text{MA}_{0.4}\text{FA}_{0.6}\text{Ba}_{0.05}\text{Pb}_{0.95}\text{I}_y\text{Cl}_{3-y}$ , and (d)  $\text{MA}_{0.4}\text{FA}_{0.6}\text{Ba}_{0.10}\text{Pb}_{0.90}\text{I}_y\text{Cl}_{3-y}$  films.

that the incorporation of Sr into perovskite film could reduce the non-radiative recombination losses [27]. The PSC with 2.0% Sr incorporation exhibited high open-circuit voltage ( $V_{oc}$ ) of nearly 1.18 V [37].

In our previous work, we partially replaced the Pb by Ba and obtained a perovskite structure of  $\text{CH}_3\text{NH}_3\text{Ba}_{1-x}\text{Pb}_x\text{I}_{3-y}\text{Cl}_y$ . The photovoltaic characteristics of PSCs based on  $\text{Ba}^{2+}$ -doped perovskite active layer are discussed thoroughly. We also studied the crystallinity, bandgap, surface microstructure and charge carrier dynamics of perovskite films systematically [38]. Therefore, the study of Ba replacing Pb has received some attention [30,39–42]. So far, how to balance the amount of Pb replacement with photovoltaic performance is still a challenge.

In this study, we fabricated the perovskite devices with  $\text{MA}_{0.4}\text{FA}_{0.6}\text{Ba}_x\text{Pb}_{1-x}\text{I}_y\text{Cl}_{3-y}$  active layer by traditional anti-solvent treatment. The crystal structure, optical property, and surface morphology of  $\text{MA}_{0.4}\text{FA}_{0.6}\text{Ba}_x\text{Pb}_{1-x}\text{I}_y\text{Cl}_{3-y}$  active layer with different doping levels were investigated. Besides, the intermediate phase of  $\text{MA}_{0.4}\text{FA}_{0.6}\text{Ba}_x\text{Pb}_{1-x}\text{I}_y\text{Cl}_{3-y}$  film is also discussed in this research by in-situ GIWAXS measurement. Finally, the PCE of  $\text{MA}_{0.4}\text{FA}_{0.6}\text{Ba}_x\text{Pb}_{1-x}\text{I}_y\text{Cl}_{3-y}$  solar cell is enhanced significantly, and the as-fabricated PSC yields a champion PCE of  $\sim 17.4\%$  without anomalous J-V hysteresis.

## 2. Experimental details

### ● Synthesis of perovskite precursor solution

For  $\text{MA}_{0.4}\text{FA}_{0.6}\text{Ba}_x\text{Pb}_{1-x}\text{I}_y\text{Cl}_{3-y}$  precursor solution (1.70 M),  $\text{CH}_3\text{NH}_3\text{I}$  (MAI, FrontMaterials)/ $\text{CH}_5\text{IN}_2$  (FAI, FrontMaterials) (molar ratio = 0.4/0.6), lead iodide ( $\text{PbI}_2$ , 99.9985%, Alfa Aesar)/lead chloride ( $\text{PbCl}_2$ , 99.999%, Sigma-Aldrich) (molar ratio = 0.9/0.1), and barium iodide ( $\text{BaI}_2$ , 99.995%, Sigma-Aldrich) with various doping concentrations are dissolved in a mixture solvent (1:1 v/v) of dimethyl sulfoxide (DMSO, 99.9%, ECHO) and  $\gamma$ -butyrolactone (GBL,  $\geq 99\%$ , Sigma-Aldrich) at 40 °C, under a continuous stirring for 24 h. The dense  $\text{TiO}_2$  precursor solution and mesoporous zinc-doped  $\text{TiO}_2$  paste were synthesized according to our previous study [43]. The hole transport layer solution was composed of 80 mg spiro-OMeTAD (FrontMaterials), 28.5  $\mu\text{L}$  4-*tert*-butylpyridine (tBP, 96%, Sigma-Aldrich), 17.5  $\mu\text{L}$  Li-TFSI solution (Li-TFSI, 99.95%, Sigma-Aldrich, 1.8 M in acetonitrile), and

1.0 mL chlorobenzene ( $\text{C}_6\text{H}_5\text{Cl}$ , CB, 99.8%, ACROS). The mixture was stirred for 30 min until spiro-OMeTAD was completely dissolved [44]. All of the solution were prepared in the humidity box ( $\sim 1.0\%$  relative humidity, 25 °C). All chemical compounds were used without any purification.

### ● Fabrication of Perovskite Devices

The FTO substrate (7  $\Omega$ , Ruilong) was cleaned by sequential sonication in detergent, acetone, and isopropanol. Then the FTO was irradiated in the UV-ozone cleaner for 30 min. The  $\text{TiO}_2$  precursor solution was coated on the FTO glass at 450 °C for 30 min by spray-coating method to form a dense  $\text{TiO}_2$  layer [45]. The dilute mesoporous zinc-doped  $\text{TiO}_2$  paste was printed on a dense  $\text{TiO}_2$  layer by screen printing method and calcined at 500 °C for 30 min. The  $\text{MA}_{0.4}\text{FA}_{0.6}\text{Ba}_x\text{Pb}_{1-x}\text{I}_y\text{Cl}_{3-y}$  precursor solution was coated onto the mesoporous zinc-doped  $\text{TiO}_2$  at 1000 and 5000 rpm for 10 and 20 sec, respectively. After 17 sec, 300  $\mu\text{L}$  of CB was dropped on top of the  $\text{MA}_{0.4}\text{FA}_{0.6}\text{Ba}_x\text{Pb}_{1-x}\text{I}_y\text{Cl}_{3-y}$  film and annealed at 100 °C for 10 min. The spiro-OMeTAD precursor solution was spin-coated onto the  $\text{MA}_{0.4}\text{FA}_{0.6}\text{Ba}_x\text{Pb}_{1-x}\text{I}_y\text{Cl}_{3-y}$  film at 4000 rpm for 30 sec. For metal electrode fabrication, 120 nm of Au electrode was thermally evaporated on the  $\text{MA}_{0.4}\text{FA}_{0.6}\text{Ba}_x\text{Pb}_{1-x}\text{I}_y\text{Cl}_{3-y}$  device with a shadow mask (0.09  $\text{cm}^2$ ).

### ● Characterization of Perovskite Materials and Devices

The surface microstructure and elemental mapping of  $\text{MA}_{0.4}\text{FA}_{0.6}\text{Ba}_x\text{Pb}_{1-x}\text{I}_y\text{Cl}_{3-y}$  film were observed by FE-SEM (su8010, HITACHI) and EDS (XFlash 5030, Bruker). The topographic image and surface roughness of  $\text{MA}_{0.4}\text{FA}_{0.6}\text{Ba}_x\text{Pb}_{1-x}\text{I}_y\text{Cl}_{3-y}$  film are analyzed by AFM (Dimension-3100 Multimode, Digital Instruments) in the tapping mode. Synchrotron-based grazing-incidence wide-angle X-ray scattering (GIWAXS) was collected by synchrotron X-ray spectroscopy ( $\lambda \sim 1.0256 \text{ \AA}$ ) on beamline 23A and 13A1 of the National Synchrotron Radiation Research Center (NSRRC) in Hsinchu, Taiwan. The absorption spectra were obtained by UV-vis spectrometer in the range 600–1000 nm (V-730, Jasco). For the PL spectra and charge carrier dynamics measurement, the data was performed as our previous report [38]. The current density-voltage (J-V) performance of the various PSCs

were measured with a Keithley 2400 m under  $100 \text{ mW/cm}^2$ , AM 1.5G sunlight illumination (YCSS-50, Yamashita) using a KG5 filtered Si as the reference cell. The device was surveyed by reverse (from 1.2 to  $-0.1 \text{ V}$ ) and forward (from  $-0.1$  to  $1.2 \text{ V}$ ) scan with the delay time of 200 ms.

### 3. Results and discussion

Fig. 1 shows the surface microstructure of various  $\text{MA}_{0.4}\text{FA}_{0.6}\text{Ba}_x\text{Pb}_{1-x}\text{I}_y\text{Cl}_{3-y}$  films with different Ba doping levels. The  $\text{MA}_{0.4}\text{FA}_{0.6}\text{PbI}_y\text{Cl}_{3-y}$  film contains small crystal grain ( $\sim 100 \text{ nm}$ ) on the surface (Fig. 1(a)). When the doping level increase to 3.0 and 5.0 mol%, the  $\text{MA}_{0.4}\text{FA}_{0.6}\text{Ba}_{0.03}\text{Pb}_{0.97}\text{I}_y\text{Cl}_{3-y}$  (Fig. 1(b)) and  $\text{MA}_{0.4}\text{FA}_{0.6}\text{Ba}_{0.05}\text{Pb}_{0.95}\text{I}_y\text{Cl}_{3-y}$  (Fig. 1(c)) films show the homogeneous surface morphology and larger crystal grain ( $\sim 350 \text{ nm}$ ). Substitution of Ba atoms with larger radius for Pb in perovskite film would affect the colloidal seed formation in the perovskite precursor solutions which is beneficial for forming a homogeneous surface morphology and high coverage [42]. As we know, larger perovskite grain and continuous film are important for high performance device [46]. At 10.0 mol% Ba doping level, the film exhibits large crystal grain ( $> 500 \text{ nm}$ ) but appears pinholes and voids (Fig. 1(d)). This may be due to the change of crystallization rate or induced non-uniform micro-strain under a large amount of Ba doping [41]. The poor coverage will deteriorate the performance of perovskite device. To further discuss the topography of various  $\text{MA}_{0.4}\text{FA}_{0.6}\text{Ba}_x\text{Pb}_{1-x}\text{I}_y\text{Cl}_{3-y}$  films, AFM was used to measure the roughness of  $\text{MA}_{0.4}\text{FA}_{0.6}\text{Ba}_x\text{Pb}_{1-x}\text{I}_y\text{Cl}_{3-y}$  film and the AFM images are shown in Fig. 2(a-d). The root mean square roughness ( $R_q$ ) of perovskite film is  $30.0 \text{ nm}$  with 5.0 mol% Ba doping, which is far smoother than pristine perovskite film ( $57.3 \text{ nm}$ ) (Fig. 2(e)). Nevertheless, due to the formation of pinholes, the  $R_q$  of  $\text{MA}_{0.4}\text{FA}_{0.6}\text{Ba}_{0.10}\text{Pb}_{0.90}\text{I}_y\text{Cl}_{3-y}$  film increased to  $42.4 \text{ nm}$ .

We examined the preferred orientation of the crystalline planes of several  $\text{MA}_{0.4}\text{FA}_{0.6}\text{Ba}_x\text{Pb}_{1-x}\text{I}_y\text{Cl}_{3-y}$  films measured by the synchrotron-based GIWAXS. Fig. 3(a-d) display a 2D scattering patterns of the samples consisted of  $\text{FTO/TiO}_2/\text{MA}_{0.4}\text{FA}_{0.6}\text{Ba}_x\text{Pb}_{1-x}\text{I}_y\text{Cl}_{3-y}$  with different Ba doping concentration. All of the samples exhibits a strong

diffraction signal for (1 1 0) and (2 2 0) plane. Remarkably, we can observe the change of preferred orientation for stacking patterns along with (1 1 0) with different Ba doping levels. Fig. 3(e) demonstrates the integrated intensity plots of the 2D scattering patterns corresponding to Fig. 3(a-d) along  $q_z$  direction. Obviously, the relative peak intensity of perovskite (1 1 0) plane increased with increasing the Ba doping concentration. These results indicate that the crystallinity of  $\text{MA}_{0.4}\text{FA}_{0.6}\text{Ba}_x\text{Pb}_{1-x}\text{I}_y\text{Cl}_{3-y}$  can be increased by Ba concentration increment. A slight doping could improve crystallinity instead of shifting the peak position [42]. Fig. 3(f) shows azimuthal intensity plots corresponding to Fig. 3(a-d) along the ring at  $q = 10 \text{ nm}^{-1}$ . The non-doped film displays higher intensity at azimuth angle of about  $23^\circ$  and  $50^\circ$  [47]. When the Ba doping level is increased, the intensity at azimuth angle of about  $23^\circ$  and  $50^\circ$  is distinctly decreased. It is worth noting that the relative peak intensity at  $90^\circ$  is increased with increasing the Ba doping level. The Ba doping into the perovskite film not only changes the crystallinity but also changes the preferred orientation of the crystalline plane.

We characterized the optical behavior of  $\text{MA}_{0.4}\text{FA}_{0.6}\text{Ba}_x\text{Pb}_{1-x}\text{I}_y\text{Cl}_{3-y}$  films with different doping level of Ba. With Ba doping, the absorption spectra of perovskite film show red-shift (Fig. 4(a)). This result is consistent with our previous study [38]. The Tauc's plots exhibit the bandgaps of the  $\text{MA}_{0.4}\text{FA}_{0.6}\text{Ba}_x\text{Pb}_{1-x}\text{I}_y\text{Cl}_{3-y}$  film with and without Ba doping (Fig. 4(b)). The bandgaps of the films were calculated via the absorption spectra. The bandgaps were 1.55, 1.54, 1.53, and 1.52 eV for 0.0, 3.0, 5.0, and 10.0 mol%, respectively. These results show that increasing Ba doping decreases the bandgap of the parent perovskite. J. Navas et al. reported that the doping agent could modify the electronic band structure with the ions in the network, resulting in the modified bandgap [48]. The change in bandgap can affect the band alignment, which affects the photovoltaic performance of perovskite device.

To reveal the effect of charge carrier extraction of  $\text{FTO/TiO}_2/\text{MA}_{0.4}\text{FA}_{0.6}\text{Ba}_x\text{Pb}_{1-x}\text{I}_y\text{Cl}_{3-y}$ , we explored the PL spectra and time-resolved PL characterization (Fig. 5(a, b)). The PL spectra of perovskite film with  $\text{TiO}_2$  quencher exhibits the decreasing trend when Ba doping level is ascending to 5.0 mol% (Fig. 5(a)). This result indicates that the perovskite film with slightly Ba doping can reduce nonradiative

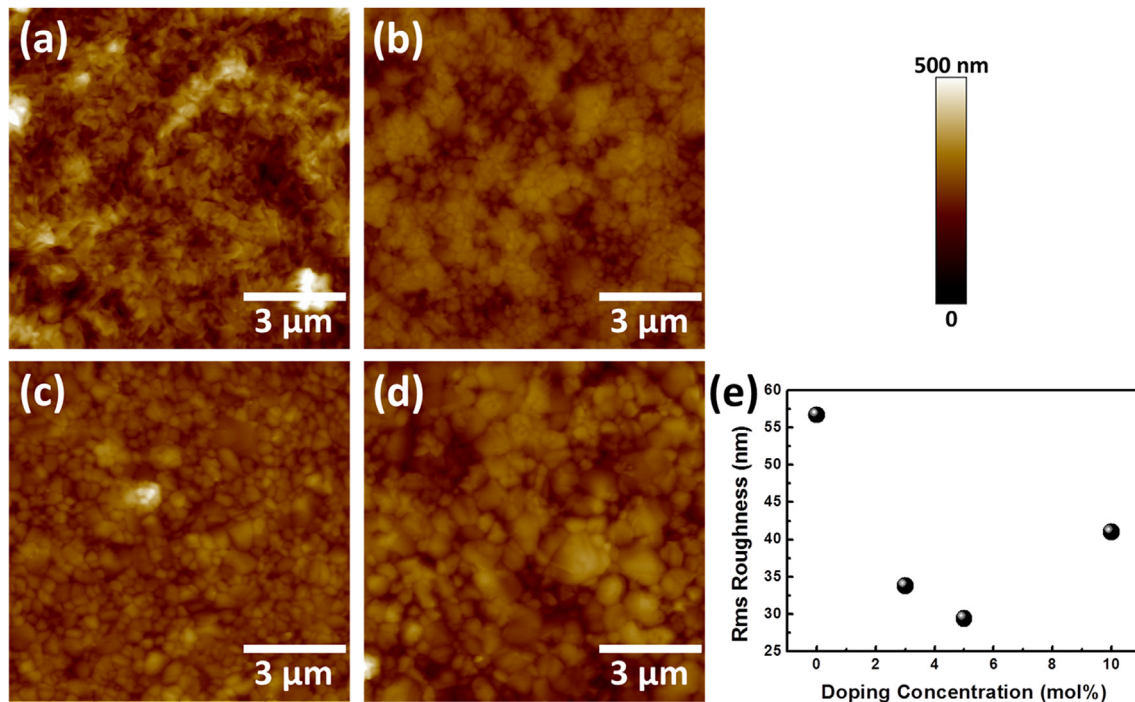
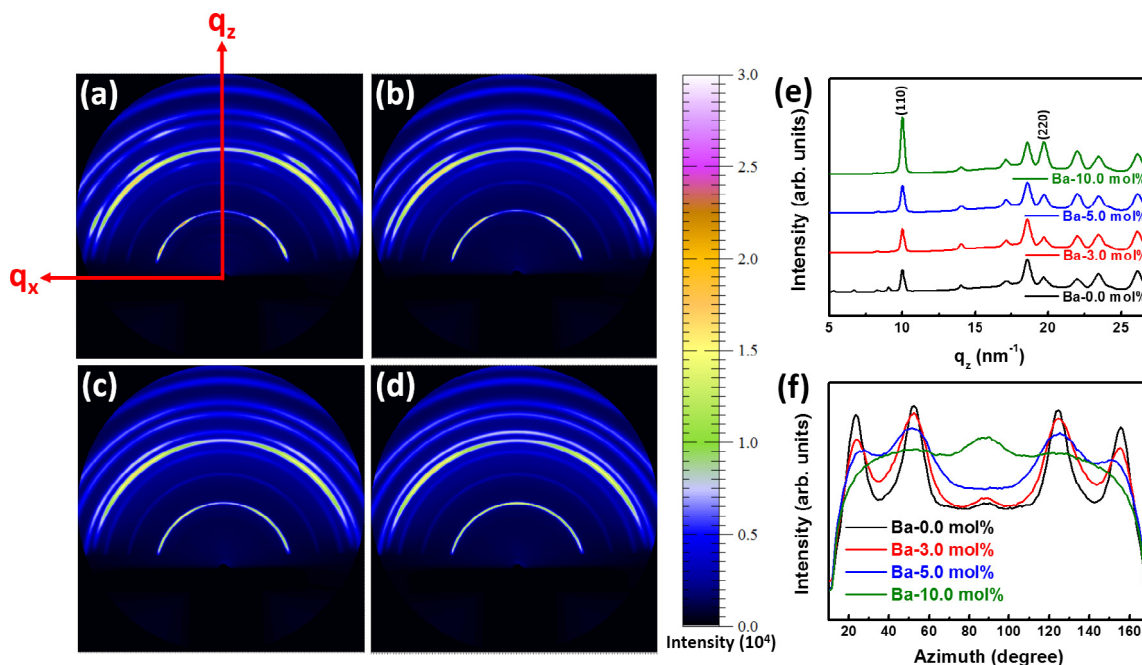


Fig. 2. AFM images of (a)  $\text{MA}_{0.4}\text{FA}_{0.6}\text{PbI}_y\text{Cl}_{3-y}$ , (b)  $\text{MA}_{0.4}\text{FA}_{0.6}\text{Ba}_{0.03}\text{Pb}_{0.97}\text{I}_y\text{Cl}_{3-y}$ , (c)  $\text{MA}_{0.4}\text{FA}_{0.6}\text{Ba}_{0.05}\text{Pb}_{0.95}\text{I}_y\text{Cl}_{3-y}$ , and (d)  $\text{MA}_{0.4}\text{FA}_{0.6}\text{Ba}_{0.10}\text{Pb}_{0.90}\text{I}_y\text{Cl}_{3-y}$  films. (e) The root-mean-square roughness of  $\text{MA}_{0.4}\text{FA}_{0.6}\text{Ba}_x\text{Pb}_{1-x}\text{I}_y\text{Cl}_{3-y}$  film with different concentration.





**Fig. 3.** (a-d) 2D GIWAXS patterns of FTO/TiO<sub>2</sub>/MA<sub>0.4</sub>FA<sub>0.6</sub>Ba<sub>x</sub>Pb<sub>1-x</sub>I<sub>y</sub>Cl<sub>3-y</sub> with different Ba doping level. (e) 1D patterns of out-of-plane line cut. (f) Azimuthal intensity plots that corresponding to Fig. 3(a-d) along the ring at  $q = 10 \text{ nm}^{-1}$ , representing the (1 1 0) plane of the MA<sub>0.4</sub>FA<sub>0.6</sub>Ba<sub>x</sub>Pb<sub>1-x</sub>I<sub>y</sub>Cl<sub>3-y</sub> film.

recombination and promote electron extraction from perovskite film to TiO<sub>2</sub> layer. The PL intensity increases again for perovskite film with 10.0 mol% Ba doping. This result evidences that excessive Ba doping can cause electron hole recombination. We further investigated the transient PL decay plots of various MA<sub>0.4</sub>FA<sub>0.6</sub>Ba<sub>x</sub>Pb<sub>1-x</sub>I<sub>y</sub>Cl<sub>3-y</sub> samples. A bi-exponential decay function was applied to fitted the TRPL decay curve [49,50],

$$F(t) = A \exp\left(-\frac{t}{\tau_1}\right) + B \exp\left(-\frac{t}{\tau_2}\right)$$

where A and B are time independent coefficient of weight fraction,  $\tau_1$  and  $\tau_2$  are fast decay lifetime and slow decay lifetime. The average decay lifetime was calculated using the following equation:

$$\tau_{\text{avg}} = (A\tau_1 + B\tau_2)/(A + B)$$

The measured  $\tau_1$ ,  $\tau_2$ , and  $\tau_{\text{avg}}$  for MA<sub>0.4</sub>FA<sub>0.6</sub>Ba<sub>x</sub>Pb<sub>1-x</sub>I<sub>y</sub>Cl<sub>3-y</sub> films are listed in Table 1. The PL decay process shows a carrier recombination process as characterized by  $\tau_2$ , as well as a injection of free carriers in the perovskite to TiO<sub>2</sub>, as characterized by  $\tau_1$  [51]. For the non-doped perovskite film,  $\tau_1$  is 21.5 ns,  $\tau_2$  is 55.7 ns and their weight fractions are

55.8% and 44.2%, respectively, leading to a  $\tau_{\text{avg}}$  of 36.6 ns. On the other hand, the  $\tau_{\text{avg}}$  of Ba doping MA<sub>0.4</sub>FA<sub>0.6</sub>Ba<sub>0.05</sub>Pb<sub>0.95</sub>I<sub>y</sub>Cl<sub>3-y</sub> film is significantly decreased to 12.5 ns. These results indicated that an enhanced charge extraction efficiency to the TiO<sub>2</sub> electron transport layer and restrained carrier recombination, and it is attributed to the compact surface microstructure and enlarged grain size of the MA<sub>0.4</sub>FA<sub>0.6</sub>Ba<sub>0.05</sub>Pb<sub>0.95</sub>I<sub>y</sub>Cl<sub>3-y</sub> film. While further increasing Ba doping ratio, the  $\tau_{\text{avg}}$  of MA<sub>0.4</sub>FA<sub>0.6</sub>Ba<sub>0.10</sub>Pb<sub>0.90</sub>I<sub>y</sub>Cl<sub>3-y</sub> film slightly elevated to 23.8 ns. The increase in PL decay lifetime is due to the increased carrier recombination fraction (30.6%).

We fabricated the PSC adopting the architecture of FTO/dense TiO<sub>2</sub>/mesoporous zinc-doped TiO<sub>2</sub>/MA<sub>0.4</sub>FA<sub>0.6</sub>Ba<sub>x</sub>Pb<sub>1-x</sub>I<sub>y</sub>Cl<sub>3-y</sub>/spiro-OMeTAD/Au electrode. Fig. S1 shows the PCE distribution of solar cells with different doping levels. The PSCs with MA<sub>0.4</sub>FA<sub>0.6</sub>Ba<sub>0.05</sub>Pb<sub>0.95</sub>I<sub>y</sub>Cl<sub>3-y</sub> active layer exhibit higher PCE. Fig. 6 is the current density-voltage (J-V) performance and photovoltaic parameters of 0.0 mol% (Fig. 6(a)), 3.0 mol% (Fig. 6(b)) 5.0 mol% (Fig. 6(c)), and 10.0 mol% (Fig. 6(d)) in both forward and reverse scan directions. The highest PCE of device-based perovskite films with 5.0 mol% Ba doping is 17.4% with a Voc of 1.09 V, Jsc of 23.5 mA/cm<sup>2</sup>. It is worth mentioning that even increasing

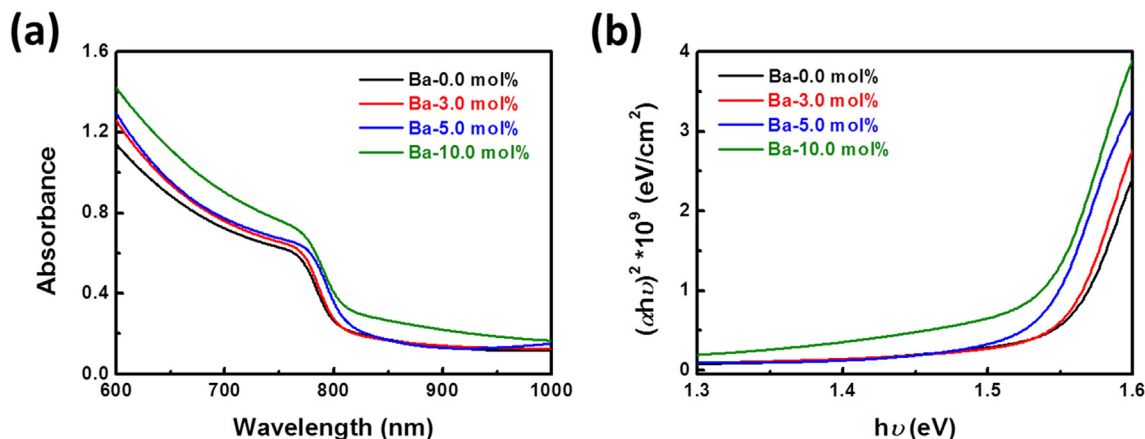


**Fig. 4.** (a) Absorption spectra and (b) Tauc's plots of the MA<sub>0.4</sub>FA<sub>0.6</sub>Ba<sub>x</sub>Pb<sub>1-x</sub>I<sub>y</sub>Cl<sub>3-y</sub> film with different doping levels.

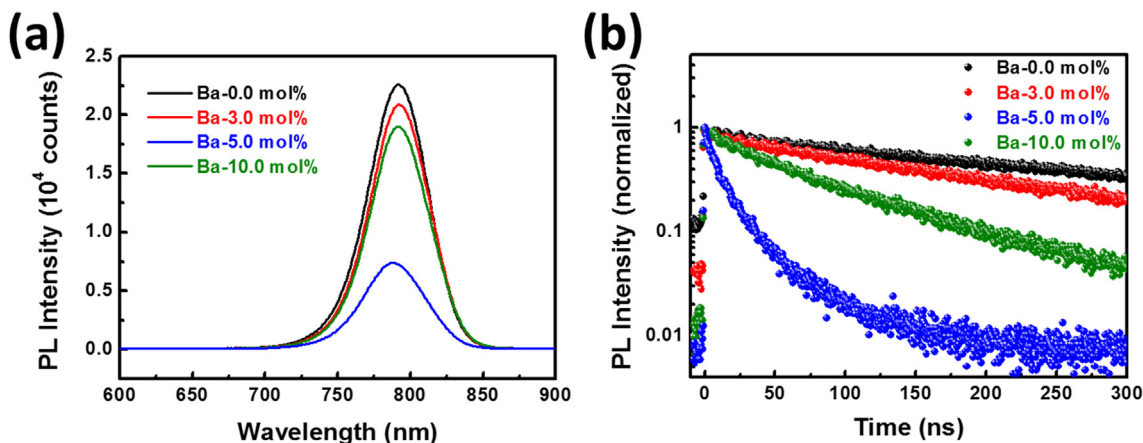


Fig. 5. (a) PL spectra, and (b) time-resolved PL characterization of the FTO/TiO<sub>2</sub>/MA<sub>0.4</sub>FA<sub>0.6</sub>Ba<sub>x</sub>Pb<sub>1-x</sub>I<sub>y</sub>Cl<sub>3-y</sub> with different doping levels.

Table 1

List of measured fast decay lifetime ( $\tau_1$ ), slow decay lifetime ( $\tau_2$ ), and average decay lifetime ( $\tau_{avg}$ ) for the film of FTO/TiO<sub>2</sub>/MA<sub>0.4</sub>FA<sub>0.6</sub>Ba<sub>x</sub>Pb<sub>1-x</sub>I<sub>y</sub>Cl<sub>3-y</sub>.

Sample Name	A (%)	$\tau_1$ (ns)	B (%)	$\tau_2$ (ns)	$\tau_{avg}$ (ns)
MA <sub>0.4</sub> FA <sub>0.6</sub> PbI <sub>y</sub> Cl <sub>3-y</sub>	55.8	21.5	44.2	55.7	36.6
MA <sub>0.4</sub> FA <sub>0.6</sub> Ba <sub>0.03</sub> Pb <sub>0.97</sub> I <sub>y</sub> Cl <sub>3-y</sub>	62.4	19.6	37.6	47.7	30.2
MA <sub>0.4</sub> FA <sub>0.6</sub> Ba <sub>0.05</sub> Pb <sub>0.95</sub> I <sub>y</sub> Cl <sub>3-y</sub>	81.0	9.4	19.0	25.6	12.5
MA <sub>0.4</sub> FA <sub>0.6</sub> Ba <sub>0.10</sub> Pb <sub>0.90</sub> I <sub>y</sub> Cl <sub>3-y</sub>	69.4	15.8	30.6	42.0	23.8

the doping concentration to 10.0 mol%, the perovskite device still maintains a performance of > 15%. For J-V hysteresis measurement, the hysteresis index (HI) of PSC with different active layer are calculated. The HI is governed by the following equation [52]:

$$HI = \frac{J_{RS}(0.8V_{oc}) - J_{FS}(0.8V_{oc})}{J_{RS}(0.8V_{oc})}$$

where  $J_{RS}(0.8V_{oc})$  and  $J_{FS}(0.8V_{oc})$  characterize current density at 80% of  $V_{oc}$  for the reverse scan and forward scan. For the perovskite layer without Ba doping, the HI is 0.036. After 5.0 mol% Ba doping, the HI decreased to 0.015, which could be assigned to the high crystallinity and flat surface morphology of the MA<sub>0.4</sub>FA<sub>0.6</sub>Ba<sub>x</sub>Pb<sub>1-x</sub>I<sub>y</sub>Cl<sub>3-y</sub> film. In

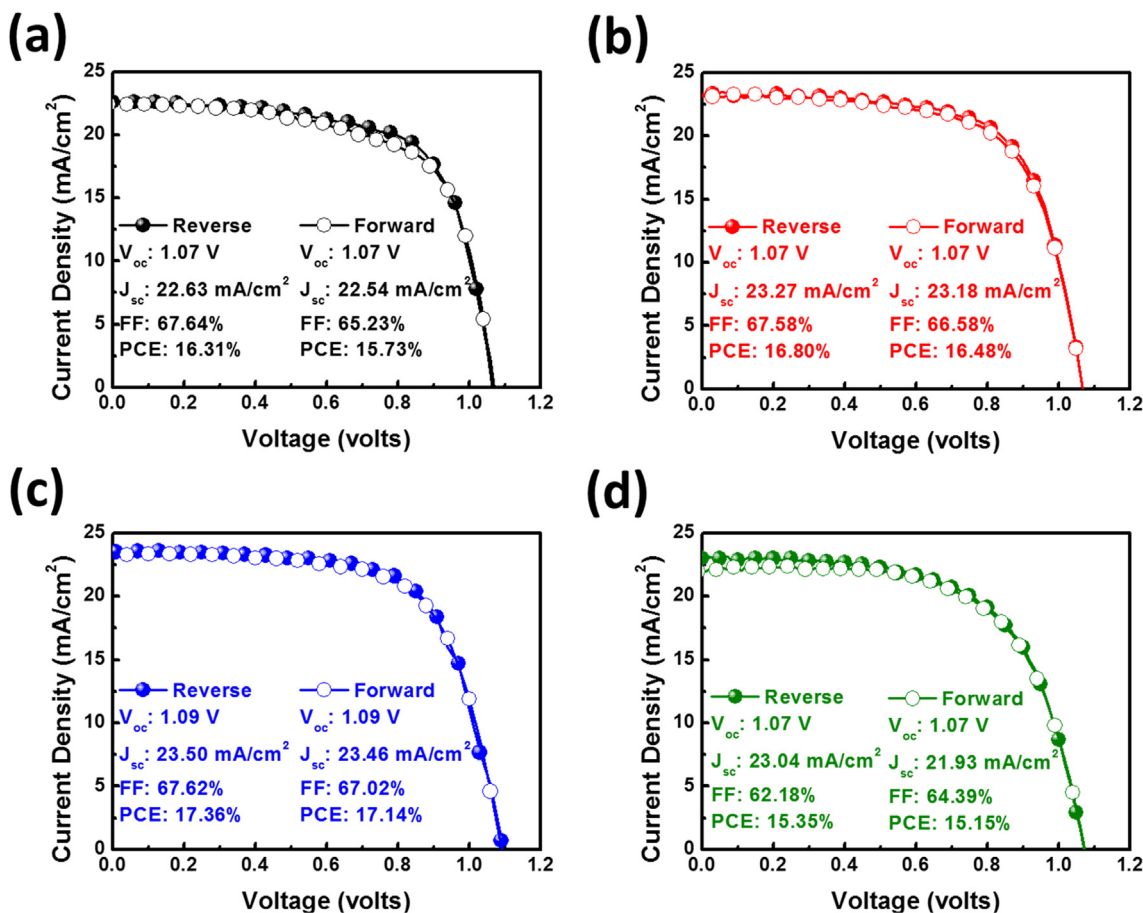


Fig. 6. J-V curves of Ba-doped PSCs with (a) 0.0 mol%, (b) 3.0 mol%, (c) 5.0 mol%, and (d) 10.0 mol% Ba-doped perovskite active layer.

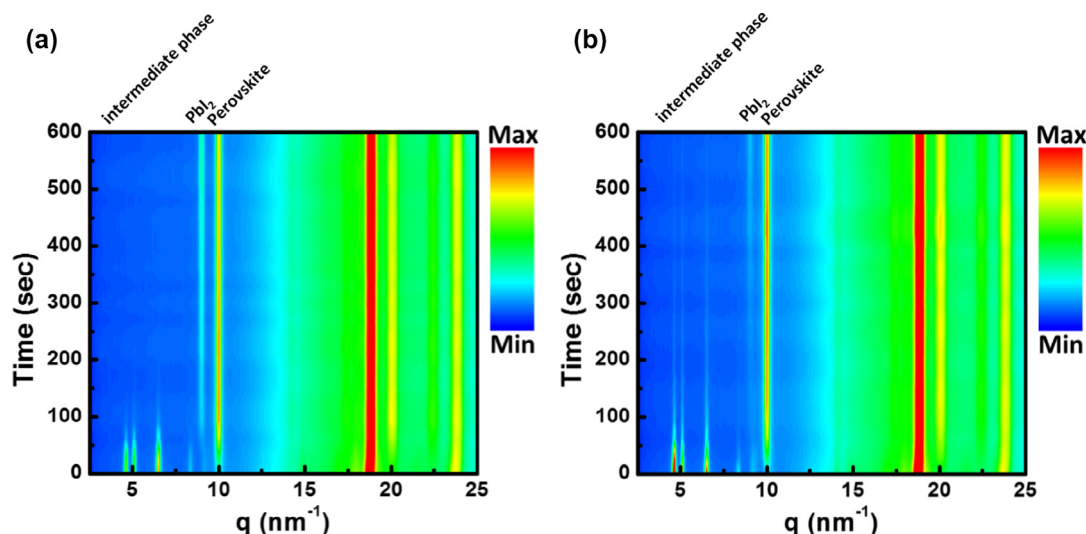


Fig. 7. In-situ GIWAXS measurements showing the crystallization process during heating process of the perovskite active layer (a) without and (b) with Ba doping.

addition, the HI slightly increased to 0.017 with 10 mol% Ba doping because the pinholes and void on perovskite film hindered the electron and hole from transferring to  $\text{TiO}_2$  electron transport layer and hole transport layer.

We have found that using Ba-doped perovskites can effectively improve efficiency and reduce hysteresis. Here we discuss the distribution of Ba element in the perovskite film. The distribution of Pb, Ba, and I was investigated by EDS mapping. Fig. S2 shows that the Pb (Fig. S2(c)), Ba (Fig. S2(d)), and I (Fig. S2(e)) are uniformly distributed on the perovskite film.

From the above analysis, we know that PSC with  $\text{MA}_{0.4}\text{FA}_{0.6}\text{Ba}_{0.05}\text{Pb}_{0.95}\text{I}_y\text{Cl}_{3-y}$  active layer exhibits higher PCE. To further investigate the effect of Ba on structural implications of the precursor solvate formation, we used in-situ GIWAXS to analyze the heating crystallization process of the perovskite layer from precursor film to solid film. The entire crystallization process can be completely recorded, and even the crystallization of the intermediate phase can be observed. Fig. 7 is the contour map of in-situ GIWAXS results. The corresponding 1D patterns (Fig. S3) are also demonstrated. Fig. 7(a) exhibits crystallization process of  $\text{MA}_{0.4}\text{FA}_{0.6}\text{PbI}_y\text{Cl}_{3-y}$ , the intermediate phase disappears in  $\sim 100$  sec, then the tetragonal perovskite phase appears. At  $\sim 300$  sec, the perovskite phase shows high crystallinity, but from 300 to 600 sec, the intensity of the perovskite phase is weakened and the intensity of the  $\text{PbI}_2$  signal is distinctly increased. This indicates that overheating causes the perovskite phase to decompose and produce  $\text{PbI}_2$  [53,54]. In contrast, perovskite film with Ba doping shows higher intermediate phase signals. At  $\sim 250$  sec, the perovskite phase shows high crystallinity and maintain high crystallinity to 600 sec. Meanwhile,  $\text{MA}_{0.4}\text{FA}_{0.6}\text{Ba}_{0.05}\text{Pb}_{0.95}\text{I}_y\text{Cl}_{3-y}$  film shows weaker signal of  $\text{PbI}_2$ . The Ba doping can effectively promote the transformation from intermediate phase to perovskite phase and suppress the formation of undesired  $\text{PbI}_2$ .

Ambient stability is a key factor that greatly affect the commercial application of perovskite devices [55–57]. For the stability test, the PSCs were stored in the ambient atmosphere ( $\sim 30\%$  relative humidity,  $25^\circ\text{C}$ ) without encapsulation. The PSCs with 0.0, 3.0, 5.0, and 10.0 mol % Ba doping concentration reached 92, 93, 99, and 91% of its initial PCE after 720 h, respectively. (Fig. 8). In addition, we also measured the light soaking stability of PSCs under AM 1.5G sunlight illumination for 2 h (Fig. S4). It can be observed that the PSC with  $\text{MA}_{0.4}\text{FA}_{0.6}\text{Ba}_{0.05}\text{Pb}_{0.95}\text{I}_y\text{Cl}_{3-y}$  shows higher stability than the PSC with  $\text{MA}_{0.4}\text{FA}_{0.6}\text{PbI}_y\text{Cl}_{3-y}$ . The PCE of the PSC with  $\text{MA}_{0.4}\text{FA}_{0.6}\text{PbI}_y\text{Cl}_{3-y}$  decreases to 61% of its initial PCE after light soaking for 2 h. In contrast, the device with  $\text{MA}_{0.4}\text{FA}_{0.6}\text{Ba}_{0.05}\text{Pb}_{0.95}\text{I}_y\text{Cl}_{3-y}$  shows the PCE

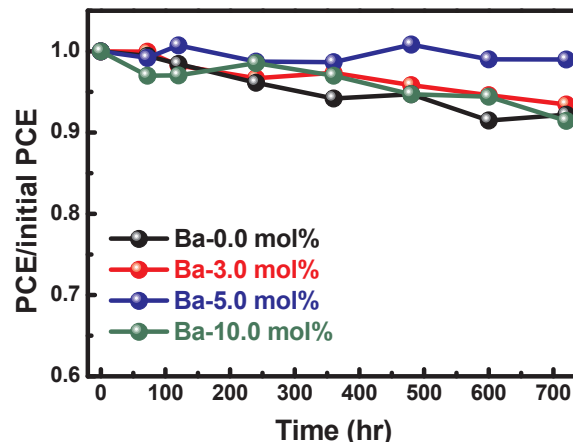


Fig. 8. Long-term stability of the  $\text{MA}_{0.4}\text{FA}_{0.6}\text{Ba}_x\text{Pb}_{1-x}\text{I}_y\text{Cl}_{3-y}$  solar cell with different doping levels under ambient atmosphere ( $\sim 30\%$  relative humidity,  $25^\circ\text{C}$ ).

degradation to 75% of the initial value. These results indicate that  $\sim 5.0$  mol% Ba doping could effectively improve crystallinity and crystallite size of perovskite film and further enhance the stability of the PSC. Moreover, the in-situ GIWAXS analysis shows that Ba doping can also improve the stability of crystal structure. This promotes the Ba-doped perovskite device with high PCE for a long time.

#### 4. Conclusion

We have successfully fabricated the PSC with  $\text{MA}_{0.4}\text{FA}_{0.6}\text{Ba}_x\text{Pb}_{1-x}\text{I}_y\text{Cl}_{3-y}$  active layer by the solvent engineering method. The optimized device was determined by optical behavior, surface morphology, and photovoltaic performance. The crystallization process of perovskite film was measured by in-situ GIWAXS to observe the effect of Ba on intermediate phase and structural stability. With 5.0 mol% Ba replacement, the optimized PCE is increased to 17.4%, the J-V hysteresis can be completely eliminated, and the device demonstrates long-term stability.

#### CRedit authorship contribution statement

**Shun-Hsiang Chan:** Methodology, Investigation, Data curation, Writing - original draft. **Ming-Chung Wu:** Writing - review & editing, Supervision. **Yi-Ying Li:** Investigation. **Kun-Mu Lee:**



Conceptualization. **Yang-Fang Chen:** Conceptualization. **Wei-Fang Su:** Project administration, Supervision.

#### Declaration of Competing Interest

The authors declare that they have no known competing financial interests or personal relationships that could have appeared to influence the work reported in this paper.

#### Acknowledgements

The authors appreciate Dr. Ming-Tao Lee group and Dr. Jyh-Fu Lee group (BL-13A1 and BL-17C) at National Synchrotron Radiation Research Center for useful discussion and suggestions. The financial support from Ministry of Science and Technology of Taiwan (Project nos. 106-2221-E-182-057-MY3, 108-3116-F-002-002-CC2, and 108-2119-M-002-005), Industrial Technology Research Institute, Chang Gung University (QZRPD181), and Chang Gung Memorial Hospital, Linkou (CMRPD2J0041 and BMRPC74) is highly appreciated.

#### Appendix A. Supplementary material

Supplementary data to this article can be found online at <https://doi.org/10.1016/j.apsusc.2020.146451>.

#### References

- [1] A. Kojima, K. Teshima, Y. Shirai, T. Miyasaka, Organometal halide perovskites as visible-light sensitizers for photovoltaic cells, *J. Am. Chem. Soc.* 131 (2009) 6050–6051.
- [2] S. Yang, S. Chen, E. Mosconi, Y. Fang, X. Xiao, C. Wang, Y. Zhou, Z. Yu, J. Zhao, Y. Gao, F. De Angelis, J. Huang, Stabilizing halide perovskite surfaces for solar cell operation with wide-bandgap lead oxysalts, *Science* 356 (2017) 1376–1379.
- [3] W.S. Yang, B.-W. Park, E.H. Jung, N.J. Jeon, Y.C. Kim, D.U. Lee, S.S. Shin, J. Seo, E.K. Kim, J.H. Noh, S.I. Seok, Iodide management in formamidinium-lead-halide-based perovskite layers for efficient solar cells, *Science* 356 (2017) 1376–1379.
- [4] H. Tan, A. Jain, O. Voznyy, X. Lan, F.P. Garcia de Arquer, J.Z. Fan, R. Quintero-Bermudez, M. Yuan, B. Zhang, Y. Zhao, F. Fan, P. Li, L.N. Quan, Y. Zhao, Z.-H. Lu, Z. Yang, S. Hoogland, E.H. Sargent, Efficient and stable solution-processed planar perovskite solar cells via contact passivation, *Science* 355 (2017) 722–726.
- [5] K.-M. Lee, M.-Y. Hou, V. Suryanarayanan, M.-C. Wu, Sequential preparation of dual-layer fluorine-doped tin oxide films for highly efficient perovskite solar cells, *ChemSusChem* 11 (2018) 3234–3242.
- [6] S.-H. Chan, Y.-H. Chang, M.-C. Wu, High-performance perovskite solar cells based on low-temperature processed electron extraction layer, *Front. Mater.* 6 (2019) 57.
- [7] Y.-R. Lin, Y.-S. Liao, H.-T. Hsiao, C.-P. Chen, Two-step annealing of niox enhances the niox-perovskite interface for high-performance ambient-stable p-i-n perovskite solar cells, *Appl. Surf. Sci.* 504 (2020) 144478.
- [8] S. Liu, Z. Wang, J. Ma, R. Ma, C. Ma, Wang, High-performance perovskite solar cells with large grain-size obtained by the synergy of urea and dimethyl sulfoxide, *Appl. Surf. Sci.* 467–468 (2019) 708–714.
- [9] H. Ye, Z. Liu, X. Liu, B. Sun, X. Tan, Y. Tu, T. Shi, Z. Tang, G. Liao, 17.78% efficient low-temperature carbon-based planar perovskite solar cells using Zn-doped SnO<sub>2</sub> electron transport layer, *Appl. Surf. Sci.* 478 (2019) 417–425.
- [10] S. Li, H. Ren, Y. Yan, Boosting efficiency of planar heterojunction perovskite solar cells to 21.2% by a facile two-step deposition strategy, *Appl. Surf. Sci.* 484 (2019) 1191–1197.
- [11] <https://www.nrel.gov/pv/assets/pdfs/best-research-cell-efficiencies.20200218.pdf>.
- [12] <https://www.healthline.com/health/lead-poisoning>.
- [13] N.K. Noel, S.D. Stranks, A. Abate, C. Wehrenfennig, S. Guarnera, A.-A. Haghighirad, A. Sadhanala, G.E. Eperon, S.K. Pathak, M.B. Johnston, A. Petrozza, L.M. Herz, H.J. Snaith, Lead-free organic-inorganic tin halide perovskites for photovoltaic applications, *Energy Environ. Sci.* 7 (2014) 3061–3068.
- [14] W. Ke, M.G. Kanatzidis, Prospects for low-toxicity lead-free perovskite solar cells, *Nat. Commun.* 10 (2019) 965.
- [15] X. Wang, T. Zhang, Y. Lou, Y. Zhao, All-inorganic lead-free perovskites for optoelectronic applications, *Mater. Chem. Front.* 3 (2019) 365–375.
- [16] J. Wang, J. Dong, F. Lu, C. Sun, Q. Zhang, N. Wang, Two-dimensional lead-free halide perovskite materials and devices, *J. Mater. Chem. A* 7 (2019) 23563–23576.
- [17] H. Fu, Review of lead-free halide perovskites as light-absorbers for photovoltaic applications: From materials to solar cells, *Sol. Energy Mater. Sol. Cells* 193 (2019) 107–132.
- [18] E. Jokar, C.-H. Chien, C.-M. Tsai, A. Fathi, E.W.-G. Diau, Robust tin-based perovskite solar cells with hybrid organic cations to attain efficiency approaching 10%, *Adv. Mater.* 31 (2019) 1804835.
- [19] E. Jokar, C.-H. Chien, A. Fathi, M. Rameez, Y.-H. Chang, E.W.-G. Diau, Slow surface passivation and crystal relaxation with additives to improve device performance and durability for tin-based perovskite solar cells, *Energy Environ. Sci.* 11 (2018) 2353–2362.
- [20] L. Wu, Z. Dong, L. Zhang, C. Liu, K. Wang, B. Zou, High-pressure band-gap engineering and metallization in the perovskite derivative Cs<sub>3</sub>Sb<sub>2</sub>I<sub>9</sub>, *ChemSusChem* 12 (2019) 3971–3976.
- [21] R. Prasanna, T. Leijtens, S.P. Dunfield, J.A. Raiford, E.J. Wolf, S.A. Swifter, J. Werner, G.E. Eperon, C. de Paula, A.F. Palmstrom, C.C. Boyd, M.F.A.M. van Hest, S.F. Bent, G. Teeter, J.J. Berry, M.D. McGehee, Design of low bandgap tin-lead halide perovskite solar cells to achieve thermal, atmospheric and operational stability, *Nat. Energy* 4 (2019) 939–947.
- [22] M. Liao, B.-B. Yu, Z. Jin, W. Chen, Y. Zhu, X. Zhang, W. Yao, T. Duan, I. Djerdj, Z. He, Efficient and stable FASnI<sub>3</sub> perovskite solar cells with effective interface modulation by low-dimensional perovskite layer, *ChemSusChem* 12 (2019) 5007–5014.
- [23] C.C. Stoumpos, Tin perovskite solar cells are back in the game, *Joule* 2 (2018) 2517–2518.
- [24] I. Kopacic, B. Friesenbichler, S.F. Hoefler, B. Kunert, H. Plank, T. Rath, G. Trimmel, Enhanced performance of germanium halide perovskite solar cells through compositional engineering, *ACS Appl. Energy Mater.* 1 (2018) 343–347.
- [25] C.F.J. Lau, X. Deng, J. Zheng, J. Kim, Z. Zhang, M. Zhang, J. Bing, B. Wilkinson, L. Hu, R. Patterson, S. Huang, A. Ho-Baillie, Enhanced performance via partial lead replacement with calcium for a CsPbI<sub>3</sub> perovskite solar cell exceeding 13% power conversion efficiency, *J. Mater. Chem. A* 6 (2018) 5580–5586.
- [26] M.-C. Wu, T.-H. Lin, S.-H. Chan, W.-F. Su, Improved efficiency of perovskite photovoltaics based on Ca-doped methylammonium lead halide, *J. Taiwan Inst. Chem. Eng.* 80 (2017) 695–700.
- [27] H. Zhang, W. Liu, R. Li, M. Zhang, M. Guo, Lead-less mesoscopic perovskite solar cells with enhanced photovoltaic performance by strontium chloride substitution, *Ceram. Int.* 44 (2018) 18863–18870.
- [28] C.F.J. Lau, M. Zhang, X. Deng, J. Zheng, J. Bing, Q. Ma, J. Kim, L. Hu, M.A. Green, S. Huang, A. Ho-Baillie, Strontium-doped low-temperature-processed CsPbI<sub>2</sub>Br perovskite solar cells, *ACS Energy Lett.* 2 (2017) 2319–2325.
- [29] M.-C. Wu, W.-C. Chen, S.-H. Chan, W.-F. Su, The effect of strontium and barium doping on perovskite-structured energy materials for photovoltaic applications, *Appl. Surf. Sci.* 429 (2018) 9–15.
- [30] W. Xiang, Z. Wang, D.J. Kubicki, X. Wang, W. Tress, J. Luo, J. Zhang, A. Hofstetter, L. Zhang, L. Emsley, M. Grätzel, A. Hagfeldt, Ba-induced phase segregation and band gap reduction in mixed-halide inorganic perovskite solar cells, *Nat. Commun.* 10 (2019) 4686.
- [31] Y. Zhou, J. Chen, O.M. Bakr, H.-T. Sun, Metal-doped lead halide perovskites: Synthesis, properties, and optoelectronic applications, *Chem. Mat.* 30 (2018) 6589–6613.
- [32] L. Liang, P. Gao, Lead-free hybrid perovskite absorbers for viable application: Can we eat the cake and have it too? *Adv. Sci.* 5 (2018) 1700331.
- [33] S. Shao, J. Liu, G. Portale, H.-H. Fang, G.R. Blake, G.H. ten Brink, L.J.A. Koster, M.A. Loi, Highly reproducible sn-based hybrid perovskite solar cells with 9% efficiency, *Adv. Energy Mater.* 8 (2018) 1702019.
- [34] L. Ji, X. Zhang, T. Zhang, Y. Wang, F. Wang, Z. Zhong, Z.D. Chen, Z. Xiao, L. Chen, S. Li, Band alignment of Pb-Sn mixed triple cation perovskites for inverted solar cells with negligible hysteresis, *J. Mater. Chem. A* 7 (2019) 9154–9162.
- [35] X. Du, R. Qiu, T. Zou, X. Chen, H. Chen, H. Zhou, Enhanced uniformity and stability of Pb-Sn perovskite solar cells via me4nbr passivation, *Adv. Mater. Interfaces* 6 (2019) 1900413.
- [36] J. Lu, D. Zhang, X. Hou, H. Gan, Z. Sun, R. Zeng, H. Chen, Q. Tian, Y. Xiong, Y. Zhang, Y. Li, Z. Zhu, Calcium doped MAPbI<sub>3</sub> with better energy state alignment in perovskite solar cells, *Appl. Phys. Lett.* 112 (2018) 193901.
- [37] P. Caprioglio, F. Zu, C.M. Wolff, J.A. Márquez Prieto, M. Stollerfoht, P. Becker, N. Koch, T. Unold, B. Rech, S. Albrecht, D. Neher, High open circuit voltages in pin-type perovskite solar cells through strontium addition, *Sustain. Energy Fuels* 3 (2019) 550–563.
- [38] S.-H. Chan, M.-C. Wu, K.-M. Lee, W.-C. Chen, T.-H. Lin, W.-F. Su, Enhancing perovskite solar cell performance and stability by doping barium in methylammonium lead halide, *J. Mater. Chem. A* 5 (2017) 18044–18052.
- [39] M.-H. Shang, J. Zhang, P. Zhang, Z. Yang, J. Zheng, M.A. Haque, W. Yang, S.-H. Wei, T. Wu, Stable bandgap-tunable hybrid perovskites with alloyed Pb-Ba cations for high-performance photovoltaic applications, *J. Phys. Chem. Lett.* 10 (2019) 59–66.
- [40] S.S. Mali, J.V. Patil, C.K. Hong, Hot-air-assisted fully air-processed barium incorporated CsPbI<sub>2</sub>Br perovskite thin films for highly efficient and stable all-inorganic perovskite solar cells, *Nano Lett.* 19 (2019) 6213–6220.
- [41] J. Bahadur, A.H. Ghahremani, S. Gupta, T. Druffel, M.K. Sunkara, K. Pal, Enhanced moisture stability of mapbI<sub>3</sub> perovskite solar cells through barium doping, *Sol. Energy* 190 (2019) 396–404.
- [42] W.S. Subhani, K. Wang, M. Du, S.F. Liu, Goldschmidt-rule-deviated perovskite CsPbI<sub>2</sub>Br by barium substitution for efficient solar cells, *Nano Energy* 61 (2019) 165–172.
- [43] M.-C. Wu, S.-H. Chan, K.-M. Lee, S.-H. Chen, M.-H. Jao, Y.-F. Chen, W.-F. Su, Enhancing the efficiency of perovskite solar cells using mesoscopic zinc-doped TiO<sub>2</sub> as the electron extraction layer through band alignment, *J. Mater. Chem. A* 6 (2018) 16920–16931.
- [44] T.L. Liu, Kelly, Perovskite solar cells with a planar heterojunction structure prepared using room-temperature solution processing techniques, *Nat. Photonics* 8 (2014) 133–138.
- [45] S.-H. Chan, S.-H. Chan, Y.-T. Lin, M.-C. Wu, Enhanced power conversion efficiency of perovskite solar cells based on mesoscopic Ag-doped TiO<sub>2</sub> electron transport

- layer, *Appl. Surf. Sci.* 469 (2019) 18–26.
- [46] Q. Guo, F. Yuan, B. Zhang, S. Zhou, J. Zhang, Y. Bai, L. Fan, T. Hayat, A. Alsaedi, Z. A. Tan, Passivation of the grain boundaries of  $\text{CH}_3\text{NH}_3\text{PbI}_3$  using carbon quantum dots for highly efficient perovskite solar cells with excellent environmental stability, *Nanoscale*, 11 (2019) 115–124.
- [47] G. Zheng, C. Zhu, J. Ma, X. Zhang, G. Tang, R. Li, Y. Chen, L. Li, J. Hu, J. Hong, Q. Chen, X. Gao, H. Zhou, Manipulation of facet orientation in hybrid perovskite polycrystalline films by cation cascade, *Nat. Commun.* 9 (2018) 2793.
- [48] J. Navas, A. Sánchez-Coronilla, J.J. Gallardo, N. Cruz Hernández, J.C. Piñero, R. Alcántara, C. Fernández-Lorenzo, D.M. De los Santos, T. Aguilar, J. Martín-Calleja, New insights into organic–inorganic hybrid perovskite  $\text{CH}_3\text{NH}_3\text{PbI}_3$  nanoparticles. An experimental and theoretical study of doping in  $\text{Pb}^{2+}$  sites with  $\text{Sn}^{2+}$ ,  $\text{Sr}^{2+}$ ,  $\text{Cd}^{2+}$  and  $\text{Ca}^{2+}$ , *Nanoscale* 7 (2015) 6216–6229.
- [49] P.-W. Liang, C.-Y. Liao, C.-C. Chueh, F. Zuo, S.T. Williams, X.-K. Xin, J. Lin, A.K.-Y. Jen, Additive enhanced crystallization of solution-processed perovskite for highly efficient planar-heterojunction solar cells, *Adv. Mater.* 26 (2014) 3748–3754.
- [50] X. Tan, X. Liu, Z. Liu, B. Sun, J. Li, S. Xi, T. Shi, Z. Tang, G. Liao, Enhancing the optical, morphological and electronic properties of the solution-processed  $\text{CsPbI}_2\text{Br}$  2 films by I doping for efficient carbon-based perovskite solar cells, *Appl. Surf. Sci.* 499 (2020) 143990.
- [51] J. Yin, J. Cao, X. He, S. Yuan, S. Sun, J. Li, N. Zheng, L. Lin, Improved stability of perovskite solar cells in ambient air by controlling the mesoporous layer, *J. Mater. Chem. A* 3 (2015) 16860–16866.
- [52] H.-S. Kim, N.-G. Park, Parameters affecting  $i-v$  hysteresis of  $\text{CH}_3\text{NH}_3\text{PbI}_3$  perovskite solar cells: Effects of perovskite crystal size and mesoporous  $\text{TiO}_2$  layer, *J. Phys. Chem. Lett.* 5 (2014) 2927–2934.
- [53] K.W. Tan, D.T. Moore, M. Saliba, H. Sai, L.A. Estroff, T. Hanrath, H.J. Snaith, U. Wiesner, Thermally induced structural evolution and performance of mesoporous block copolymer-directed alumina perovskite solar cells, *ACS Nano* 8 (2014) 4730–4739.
- [54] C.-Y. Chang, Y.-C. Huang, C.-S. Tsao, W.-F. Su, Formation mechanism and control of perovskite films from solution to crystalline phase studied by in situ synchrotron scattering, *ACS Appl. Mater. Interfaces* 8 (2016) 26712–26721.
- [55] Y. Wei, K. Yao, X. Wang, Y. Jiang, X. Liu, N. Zhou, F. Li, Improving the efficiency and environmental stability of inverted planar perovskite solar cells via silver-doped nickel oxide hole-transporting layer, *Appl. Surf. Sci.* 427 (2018) 782–790.
- [56] Y. Hu, S. Zhang, W. Ruan, D. Wang, Y. Wu, F. Xu, Interfacing pristine  $\text{BiI}_3$  onto  $\text{TiO}_2$  for efficient and stable planar perovskite solar cells, *Appl. Surf. Sci.* 144769 (2019).
- [57] J.M. Kim, C.W. Jang, J.H. Kim, S. Kim, S.-H. Choi, Use of  $\text{AuCl}_3$ -doped graphene as a protecting layer for enhancing the stabilities of inverted perovskite solar cells, *Appl. Surf. Sci.* 455 (2018) 1131–1136.